catalysts

MDPI

Article

A Novel Organic/Inorganic Dual Z-Scheme Photocatalyst with Visible-Light Response for Organic Pollutants Degradation

Taoming Yu [1,†], Doudou Wang [1,†], Lili Li [1], Wenjing Song [1], Xuan Pang [2,*] and Ce Liang [1,*]

[1] Key Laboratory of Automobile Materials, Ministry of Education, College of Materials Science and Engineering, Jilin University, Changchun 130022, China; ytm19990602@163.com (T.Y.); wangdd166@163.com (D.W.); lilyllee@jlu.edu.cn (L.L.); wjsong_22@163.com (W.S.)
[2] Key Laboratory of Polymer Ecomaterials, Changchun Institute of Applied Chemistry, Chinese Academy of Sciences, Changchun 130022, China
* Correspondence: xpang@ciac.ac.cn (X.P.); liangce@jlu.edu.cn (C.L.)
† These authors contributed equally to this work.

Abstract: The design of highly efficient organic/inorganic photocatalysts with visible-light response has attracted great attention for the removal of organic pollutants. In this work, the polyacrylonitrile (PAN) worked as the matrix polymer, while polyaniline (PANI) and Sb_2S_3–ZnO were used as organic/inorganic photocatalysts. The heterojunction PAN/PANI–Sb_2S_3–ZnO photocatalyst was prepared using electrospinning and surface ultrasound. PAN/PANI–Sb_2S_3–ZnO exhibited an excellent visible-light absorption intensity in the wavelength range of 400–700 nm. The maximum removal efficiencies of PAN/PANI–Sb_2S_3–ZnO for four organic dyes were all greater than 99%. The mechanism study showed that a dual Z-scheme could be constructed ingeniously because of the well-matched bandgaps between organic and inorganic components in the photocatalyst, which achieved efficient separation of photogenerated carriers and reserved photogenerated electrons (e^-) and holes (h^+) with strong redox ability. The active species •OH and $•O_2^-$ played an important role in the photocatalytic process. The composite photocatalyst also had excellent stability and reusability. This work suggested a pathway for designing novel organic/inorganic composite photocatalysts with visible-light response.

Keywords: photocatalyst; Sb_2S_3; PANI; ZnO

Citation: Yu, T.; Wang, D.; Li, L.; Song, W.; Pang, X.; Liang, C. A Novel Organic/Inorganic Dual Z-Scheme Photocatalyst with Visible-Light Response for Organic Pollutants Degradation. *Catalysts* **2023**, *13*, 1391. https://doi.org/10.3390/catal13111391

Academic Editor: Giuseppe Mele

Received: 19 September 2023
Revised: 18 October 2023
Accepted: 21 October 2023
Published: 24 October 2023

1. Introduction

With the rapid development of industrialization, the discharge of dye wastewater has become one of the main sources of water pollution, which brings serious harm to the ecological environment and human health [1–3]. Photocatalysis has been widely studied for its low energy consumption, low cost, and absence of secondary pollution among many organic dye treatment methods [4]. However, the common inorganic photocatalysts have a narrow spectral absorption range and low utilization rate of visible light, which severely limits their wide application [5]. Hence, developing highly efficient visible-light-driven photocatalysts for environmental remediation has become an active research area.

In recent years, the organic conjugated polymers have attracted extensive attention from researchers because of their excellent visible-light absorption range, adjustable band gap, and great advantages compared with small molecules in forming and processing, which opens up broader application prospects for the development of photocatalysts [5–7]. The delocalized π–π conjugated structures have been proven to induce a wide spectral absorption range, which is beneficial to improve the fraction of the visible light used [8]. Among these delocalized conjugated materials, polyaniline (PANI) is a potential photocatalytic material due to its unique electrical conductivity, facile preparation, and chemical stability [9]. When PANI is exposed to light, the energy absorbed by electrons transitions

from highest unoccupied molecular orbital (HOMO) to lowest unoccupied molecular orbital (LOMO) produced photogenic e^--h^+ pairs [10–12]. The presence of e^- or h^+ at the impurity level can improve the electrical conductivity of PANI, showing a photoelectric conversion effect.

However, the single component photocatalyst is always limited by the quick combination of photo-generated e^- and h^+, which results in a poor quantum efficiency and low photocatalytic activity [13–15]. To date, many efforts, such as non-metal doping, facet control, surface sensitization, and heterojunction construction, have been applied to limit the recombination of photogenerated carriers [16–19]. Among these approaches, heterojunction photocatalysts have been fabricated extensively to enhance the separation efficiency of photoexcited electron–hole pairs [20–22]. Ge et al. reported the preparation of g-C_3N_4/PANI composite photocatalysts, which displayed an enhanced photocatalytic activity for the photodegradation of methylene blue (MB) dye [23]. Wang et al. synthesized the PANI/BiOCl composite photocatalyst via BiOCl modified using PANI [24]. The photocatalytic activity of PANI/BiOCl composites was greater than BiOCl, which could be assigned to the synergistic effect between PANI and BiOCl. Sb_2S_3 and ZnO are also common inorganic photocatalysts. Sb_2S_3 has the advantages of a low cost, suitable band gap (1.5–2.2 eV), good visible-light absorption capacity and charge transport performance [25–27]. ZnO, with a band gap of 3.2 eV, has the advantage of a strong redox capacity of its photogenerated charge carriers [28–30]. It could be seen that the band structures of Sb_2S_3 and ZnO were both well-matched with PANI, so a heterojunction might be formed among PANI, Sb_2S_3, and ZnO. Membrane photocatalysts have emerged as a powerful and attractive way to remove dyes from water resources. Compared with a coating film, electrospinning has been increasingly employed in fabricating nanofiber membranes with high porosity and a large specific-surface area [31]. Meanwhile, the dispersity of functional nanoparticles on membrane photocatalysts could influence the photocatalytic performance of photocatalysts. Surface ultrasound is an effective method that can achieve uniform dispersion of functional particles on the membrane surface [32].

Herein, a dual Z-scheme photocatalyst of PAN/PANI–Sb_2S_3–ZnO was designed using electrospinning and surface ultrasound. The chemical structures, morphologies, and optical and electrochemical performance of photocatalysts were systemically analyzed. The photocatalytic performance of PAN/PANI–Sb_2S_3–ZnO was evaluated using the degradation of organic dyes under visible-light irradiation. The main active species were explored using free radical trapping experiments. Furthermore, a novel dual Z-scheme photocatalytic mechanism was proposed.

2. Results and Discussion

2.1. The Structure of the Composite Membranes

The FTIR spectra of PAN/PANI, PAN/PAN/PANI–Sb_2S_3, and PAN/PANI–Sb_2S_3–ZnO are shown in Figure 1. The characteristic peak at 1450 cm^{-1} was attributed to the tensile vibration of benzene ring C=C in PANI [33]. The peak at 1029 cm^{-1} was the vibration of C–H bonds on disubstituted benzene in the PANI [33]. The peak at 2943 cm^{-1} corresponded to the tensile vibration peak of $–CH_2$ in PAN. The peak at 1308 cm^{-1} was attributed to the in-plane flexural vibration of CH_2 in PAN. Compared with PAN/PANI, both PAN/PANI–Sb_2S_3 and PAN/PANI–Sb_2S_3–ZnO showed a new characteristic peak at 630 cm^{-1}, which was mainly attributed to the formation of Sb–S bonds, proving that Sb_2S_3 was successfully doped in PAN/PANI [34]. However, the tensile vibration of the Zn–O bond at 443 cm^{-1} in the fingerprint region [35] was not observed in PAN/PANI–Sb_2S_3–ZnO.

Figure 2 shows the XRD pattern of the samples. A diffraction peak appeared at the 2θ of 25.5°, corresponding to the semi-crystalline structure of the PANI [36]. The diffraction peaks appeared at 2θ of 40.6°, 43.8°, 46.6°, 49.1°, 65.6°, and 71.0° in PAN/PANI–Sb_2S_3, which was attributed to the (611), (323), (631), (513), (624), and (045) crystal planes of Sb_2S_3. Compared with PAN/PANI–Sb_2S_3, the PAN/PANI–Sb_2S_3–ZnO showed new diffraction peaks at 31.7°, 34.4°, 36.2°, 47.5°, 56.6°, 62.9°, 67.9°, 69.1°, and 76.9°, which corresponded

to the (100), (002), (101), (102), (110), (103), (112), (201), and (202) crystal planes of ZnO. The results showed that PAN/PANI–Sb_2S_3–ZnO had been successfully prepared [37].

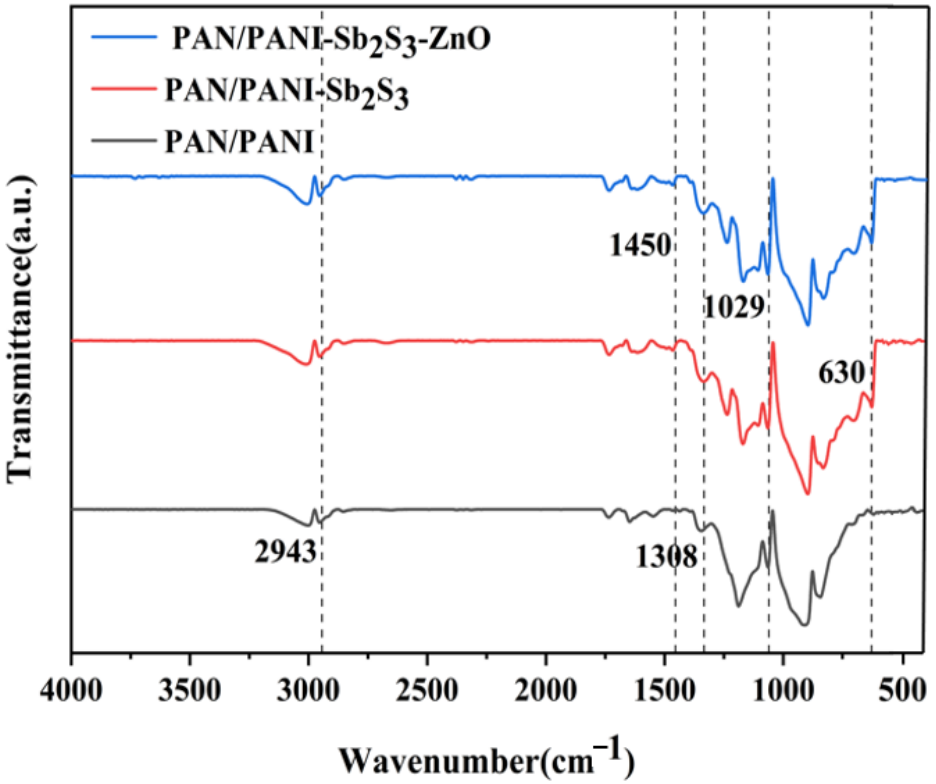

Figure 1. FTIR spectra of composite membranes.

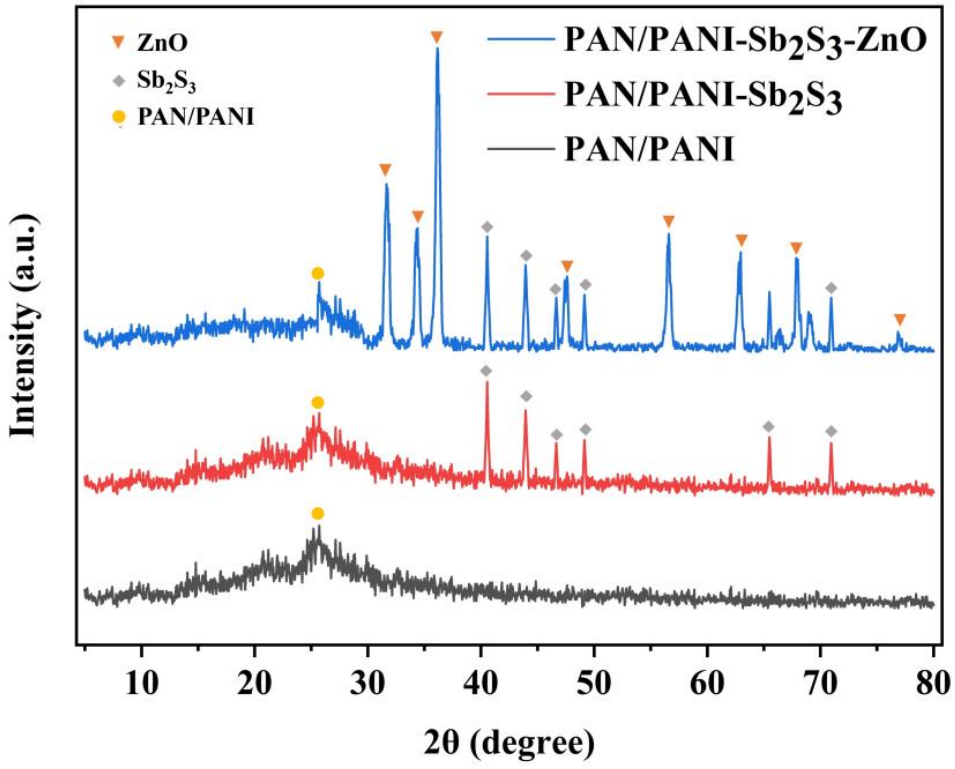

Figure 2. XRD spectra of composite membranes.

The surface chemical components of PAN/PANI, PAN/PANI–Sb_2S_3 and PAN/PANI–Sb_2S_3–ZnO composites were further analyzed using XPS. Figure 3 shows the full XPS spectra of the photocatalysts. It could be observed that the peaks appeared at 286 eV, 400 eV, and 531 eV, which corresponded to the peaks of C 1s, N 1s, and O 1s, respectively. The new peaks at 170 eV and 498 eV for PAN/PANI–Sb_2S_3 corresponded to the S 2p and Sb 3d peaks [38]. Compared with PAN/PANI–Sb_2S_3, PAN/PANI–Sb_2S_3–ZnO had new peaks at 11 eV, 89 eV, 139 eV, and 1022 eV, which were attributed to the Zn 3d, Zn 3p, Zn 3s, and Zn 2p, respectively [39]. The dispersion of ZnO on the surface of the fiber membrane was proved.

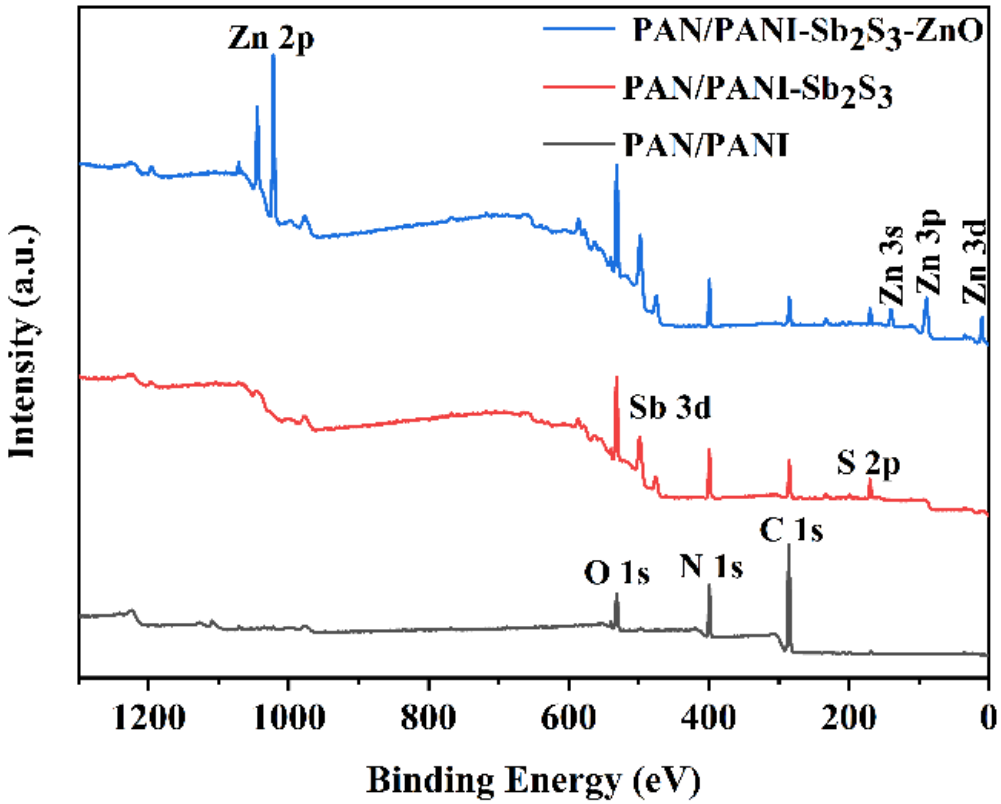

Figure 3. XPS full spectra of composite membranes.

Figure 4a shows the high-resolution XPS spectra of the C 1s of PAN/PANI–Sb_2S_3–ZnO. The peaks at 284.8 eV, 286.6 eV, and 288.6 eV corresponded to the C–H/C–C, C–N and C=N [40]. The N 1s spectra was shown in Figure 4b. The peaks at 399.5 eV and 401.7 eV represented the –NH and $–N^+$ = structure [36]. The high-resolution spectra of O 1 s is shown in Figure 4c, where the peak at 530.4 eV was attributed to oxygen ions in the Zn–O bond and the peak at 532.3 eV was attributed to the presence of a C=O bond. Figure 4d illustrates the spectra of Sb 2p. The peaks at 539.7 eV and 531.1 eV corresponded to Sb^{3+} 3d 3/2 and Sb^{3+} 3d 5/2, respectively [41]. Figure 4e shows the high-resolution spectra of S 2p. The peaks at 163.1 and 162.1 eV were attributed to S 2p 1/2 and S 2p 3/2, respectively [41]. The high-resolution spectra of Zn 2p are shown in Figure 4f, where the peaks at 1045.1 eV and 1021.9 eV corresponded to Zn 2p 1/2 and Zn 2p 3/2, respectively [42].

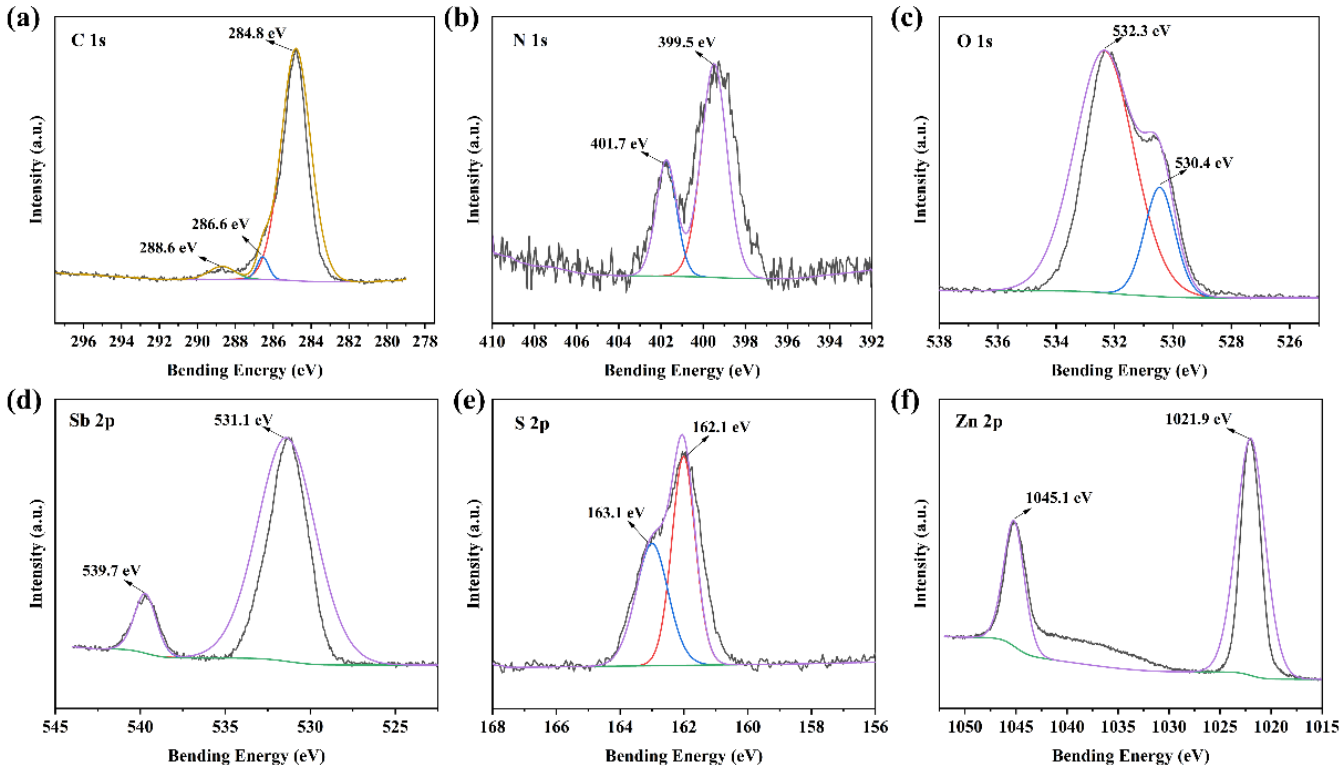

Figure 4. XPS high-resolution spectra of (**a**) C 1s, (**b**) N 1s, (**c**) O 1s, (**d**) Sb 2p, (**e**) S 2p, (**f**) Zn 2p of PAN/PANI–Sb_2S_3–ZnO.

2.2. The Morphologies of the Composite Membrane

Figure 5a shows an SEM image of the PAN/PANI. It could be seen that PAN/PANI fibers had a relatively uniform diameter distribution. In Figure 5b, PAN/PANI–Sb_2S_3 fibers were continuous and uniform, and the spheroidal Sb_2S_3 was dispersed on the fiber surface. Compared with PAN/PANI–Sb_2S_3, ZnO nanoparticles with a smaller diameter were evenly distributed along the fibers PAN/PANI–Sb_2S_3–ZnO (Figure 5c).

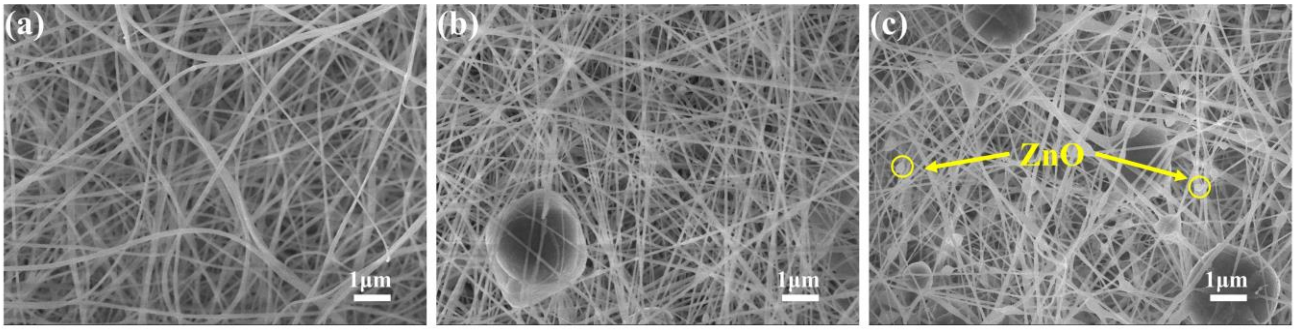

Figure 5. SEM images of (**a**) PAN/PANI, (**b**) PAN/PANI–Sb_2S_3, and (**c**) PAN/PANI–Sb_2S_3–ZnO.

A TEM image of the PAN/PANI–Sb_2S_3–ZnO composite membrane is depicted in Figure 6a. It could be seen that both Sb_2S_3 and ZnO had good interfacial contact with fibers. Figure 6b–g showed the EDS images of PAN/PANI–Sb_2S_3–ZnO. The distributions of the C, N, and O elements were uniformly dispersed. The distributions of the S, Sb, and Zn elements were consistent with the distributions of Sb_2S_3 and ZnO in the TEM image, which further proved the heterogeneous structures of composite photocatalysts.

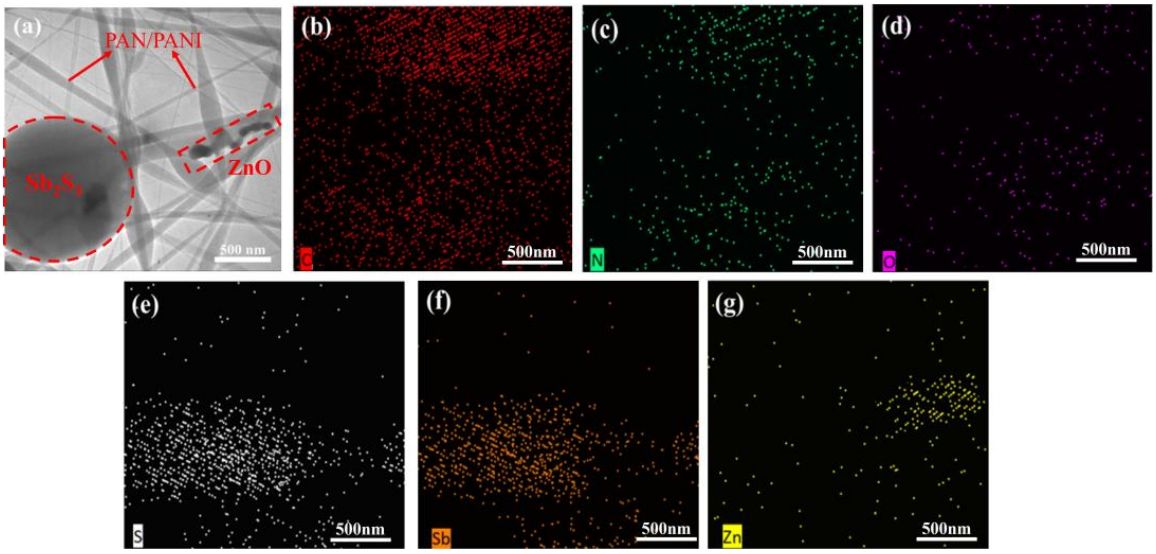

Figure 6. TEM (**a**) and EDS (**b**–**g**) images of the PAN/PANI–Sb_2S_3–ZnO membrane.

2.3. The Optical and Electrochemical Properties of Composite Membranes

The UV-vis DRS was used to analyze the optical properties of PAN/PANI, PAN/PANI–Sb_2S_3, and PAN/PANI–Sb_2S_3–ZnO (shown in Figure 7). It could be observed that all the samples showed a strong absorption capacity in the wavelength range of 400–700 nm. This was mainly due to the π-conjugated structures in the PANI molecular chain, which could provide a wide spectrum absorption range and high absorption coefficient [43–45]. It was worth noting that the light absorption intensity of the photocatalyst decreased with the addition of Sb_2S_3 and ZnO.

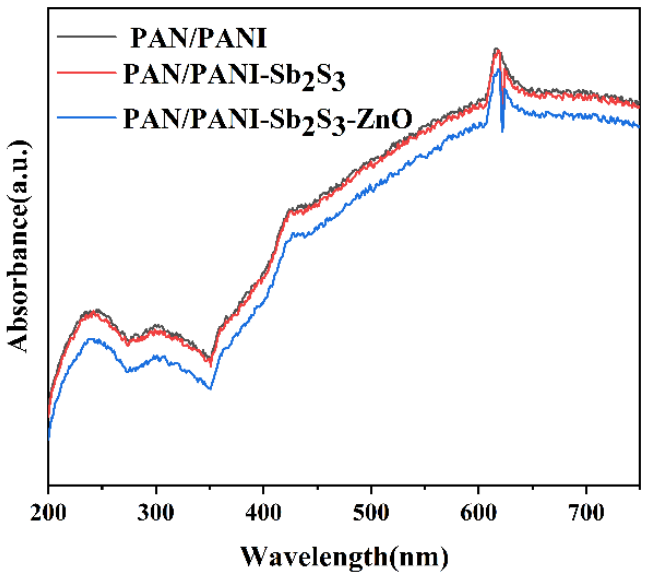

Figure 7. UV-vis DRS spectra of PAN/PANI, PAN/PANI–Sb_2S_3 and PA; N/PANI–Sb_2S_3–ZnO.

The carrier separation efficiencies of PAN/PANI, PAN/PANI–Sb_2S_3, and PAN/PANI–Sb_2S_3–ZnO were analyzed using PL spectroscopy, as shown in Figure 8a. It was observed that PAN/PANI exhibited a strong fluorescence peak, indicating that PAN/PANI had a high e^-h^+ recombination rate under light. The fluorescence peak of PAN/PANI–Sb_2S_3 was lower than that of PAN/PANI, indicating that the recombination of photogenerated carriers was inhibited after the addition of Sb_2S_3. The main reason for this was that PANI and Sb_2S_3 formed an effective heterojunction structure, which promoted carrier migration.

PAN/PANI–Sb_2S_3–ZnO exhibited the weakest fluorescence peak, which indicated that the addition of ZnO further inhibited the recombination of carriers and promoted the separation of e^- and h^+. Time-resolved photoluminescence spectra (TRPS) were used to investigate carrier lifetime. τ_1 and τ_2 represented the lifetimes of radioactive and nonradioactive charges. As shown in Figure 8b, the average lifetimes (τ) of PAN/PANI, PAN/PANI–Sb_2S_3, and PAN/PANI– Sb_2S_3–ZnO were 4.91, 5.02, and 5.45 ns, respectively. The average carrier lifetime of PAN/PANI–Sb_2S_3–ZnO was longer than that of PAN/PANI and PAN/PANI–Sb_2S_3, which proved that PAN/PANI–Sb_2S_3–ZnO had the highest separation efficiency for photogenerated charge carriers.

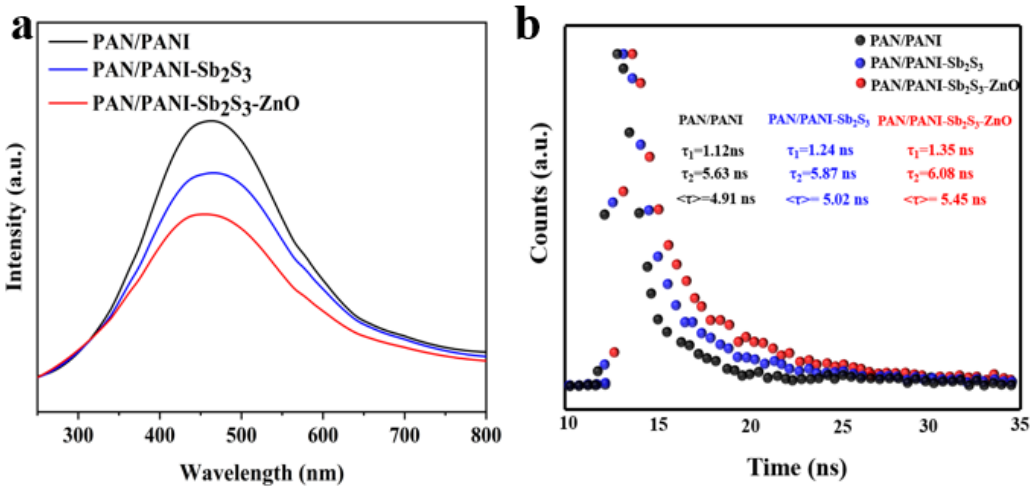

Figure 8. (**a**) PL spectra of PAN/PANI, PAN/PANI–Sb_2S_3, and PAN/PANI–Sb_2S_3–ZnO; and (**b**) TRPS of PAN/PANI, PAN/PANI–Sb_2S_3, and PAN/PANI–Sb_2S_3–ZnO.

2.4. Evaluation of Removal Performance of Organic Dyes

Figure 9 shows the kinetic curves for RhB with the PAN/PANI, PAN/PANI–Sb_2S_3, and PAN/PANI–Sb_2S_3–ZnO under simulated sunlight irradiation. Under 40 min simulated sunlight irradiation, the degradation efficiency of RhB dye with PAN/PANI was only 37.39%, indicating that PANI with a conjugated structure had the lowest photocatalytic degradation efficiency. After adding Sb_2S_3, the photocatalytic degradation efficiency of PAN/PANI–Sb_2S_3 increased to 85.41%. The remarkable improvement of photocatalytic performance might be because of the promoted carrier separation efficiency of the heterojunction structure in PAN/PANI–Sb_2S_3. The degradation efficiency of RhB dye with PAN/PANI–Sb_2S_3–ZnO further improved to 99.2%. The corresponding kinetic parameters are shown in Table S1. The determination coefficient values (R^2) proved that the photocatalytic reaction process of the composites was consistent with the pseudo-first order kinetic model [46,47]. The k_{app} values for PAN/PANI, PAN/PANI–Sb_2S_3, and PAN/PANI–Sb_2S_3–ZnO were 0.0323, 0.0429 and 0.0598 min^{-1}, respectively. The PAN/PANI–Sb_2S_3–ZnO had a maximum k_{app} value and the lowest $t_{1/2}$, which clarified the fastest photocatalytic degradation rate. Considering that the self-degradation of organic dyes, amoxicillin was selected as the target pollutant to further explore the photocatalytic degradation ability of PAN/PANI–Sb_2S_3–ZnO (see Figure S1). Under simulated sunlight irradiation for 40 min, the degradation efficiency of amoxicillin using PAN/PANI was only 38.12%. After adding Sb_2S_3, the photocatalytic degradation efficiency increased to 86.45%. The highest degradation efficiency of amoxicillin was obtained using PAN/PANI–Sb_2S_3–ZnO, with 94.13% degraded. The results showed that PAN/PANI–Sb_2S_3–ZnO had the best photodegradation ability for the pollutants.

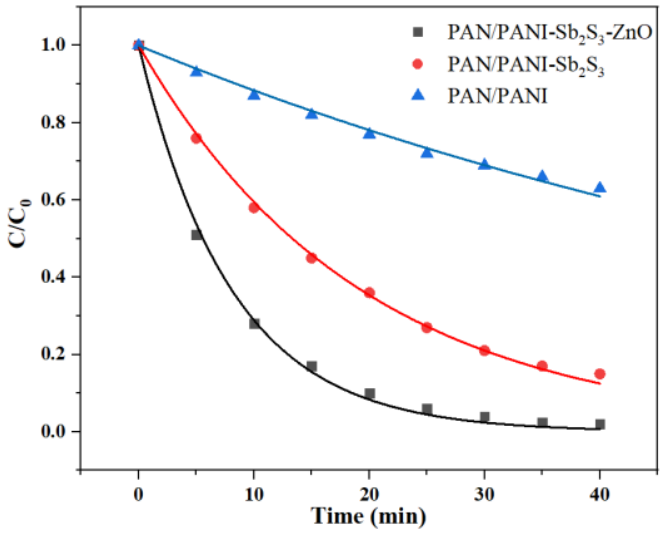

Figure 9. Kinetic curves from pseudo-first order kinetic model fitted to the experimental data of RhB photodegradation reaction using PAN/PANI, PAN/PANI–Sb_2S_3, and PAN/PANI–Sb_2S_3–ZnO.

Figure 10a shows the effect of pH on the degradation of RhB, MB, MO, and CR using PAN/PANI–Sb_2S_3–ZnO. With an increase in the pH value, the removal efficiency of RhB and MB improved and the removal efficiency of MO and CR decreased. The maximum removal efficiencies of 99.81% and 96.42% were achieved for RhB and MB at pH = 10.0, and the maximum removal efficiencies of 86.77% and 80.54% were achieved for MO and CR at pH = 2.0. As presented in Figure 10b, the isoelectric point of the PAN/PANI–Sb_2S_3–ZnO membrane was at pH = 5.0 (pH_{pzc} = 5.0). When pH < pH_{pzc}, PAN/PANI–Sb_2S_3–ZnO was positively charged. The removal efficiencies of anionic dyes were relatively high because of the electrostatic attraction between PAN/PANI–Sb_2S_3–ZnO and anionic dye. When pH > pH_{pzc}, PAN/PANI–Sb_2S_3–ZnO was negatively charged. The removal efficiencies of cationic dyes were relatively high because of the electrostatic attraction between PAN/PANI–Sb_2S_3–ZnO and cationic dye.

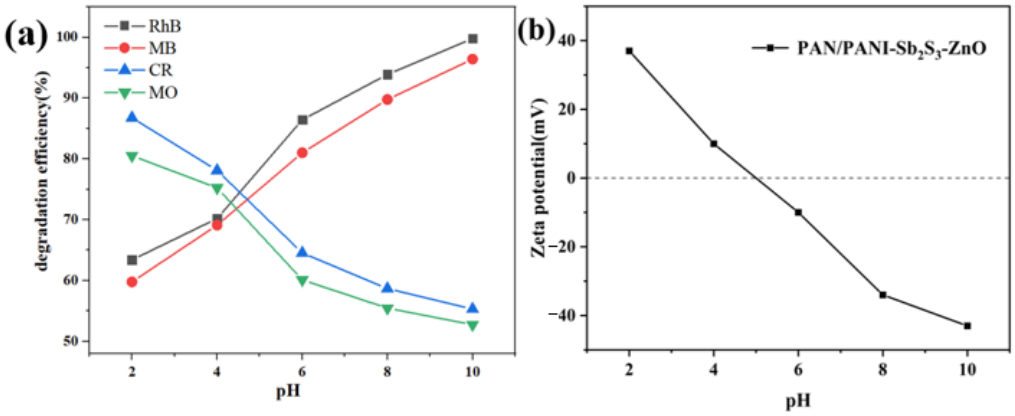

Figure 10. (**a**) Photocatalytic degradation efficiency of PAN/PANI–Sb_2S_3–ZnO photocatalyst for RhB, MB, CR and MO at different pH values and (**b**) dependence of the Zeta potential of the PAN/PANI–Sb_2S_3–ZnO membrane surface on pH.

Figure 11 shows the kinetic curves for RhB, MB, CR, and MO using PAN/PANI–Sb_2S_3–ZnO. Under 40 min simulated sunlight irradiation, the degradation efficiencies of PAN/PANI–Sb_2S_3–ZnO for RhB, MB, CR, and MO were 99.8%, 96.42%, 86.77%, and 78.54%. Obviously, the degradation efficiencies of PAN/PANI–Sb_2S_3–ZnO for cationic dyes (RhB and MB) were higher than those of anionic dyes (CR and MO). This was because the pH values of the four organic dye solutions were all greater than the pH_{pzc} of PAN/PANI–

Sb_2S_3–ZnO, so the membrane was electronegative in the dye solutions. Under the effect of electrostatic attraction, the negatively charged PAN/PANI–Sb_2S_3–ZnO was more favorable to fully contact with cationic dyes, which was conducive to the photocatalytic degradation process. The corresponding kinetic parameters are shown in Table S2. The k_{app} values of cationic RhB and MB were higher than those of anionic CR and MO, which further proved that PAN/PANI–Sb_2S_3–ZnO had a higher photocatalytic degradation rate for cationic dyes. PAN/PANI–Sb_2S_3–ZnO exhibited a higher photodegradation rate for RhB and MB than other reported heterostructure photocatalysts, as depicted in Table S3.

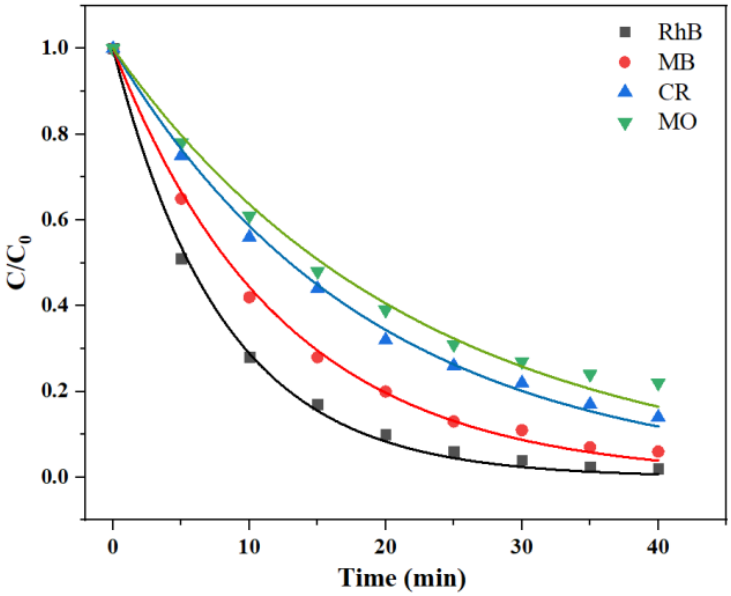

Figure 11. Kinetic curves from pseudo-first order kinetic model fitted to the experimental data of RhB, MB, CR, and MO photodegradation reaction under photocatalytic degradation using PAN/PANI–Sb_2S_3–ZnO. [Reaction conditions: initial concentration = 12 mg/L, photocatalyst = 0.2 g, pH value for MO and CR solutions = 2, pH value for RhB and MB solutions = 10, t = 40 min, simulated sunlight irradiation].

The Langmuir–Hinshelwood (L–H) model (presented in Supplementary Materials) was used to study the photodegradation kinetics of different initial concentrations of RhB using PAN/PANI–Sb_2S_3–ZnO. The validated linear relation for curves of $\ln(C_0/C_t)$ versus t are shown in Figure S1. The kinetic parameters of photocatalytic degradation are shown in Table S4, and the correlation coefficients (R^2) were all greater than 0.98. It could be seen that the k_{app} values decreased with the increasing initial concentration, which was possibly due to the difficulty of penetration of light irradiations into a large concentration gradient. When the initial concentration was 12 mg/L, the k_{app} values were the greatest.

The UV-vis absorbance changes of RhB, MB, CR, and MO dye solutions at different photocatalytic times are illustrated in Figure 12. The maximum UV-vis absorbances for RhB, MB, MO, and CR at 554 nm, 664 nm, 497 nm, and 460 nm were 2.2505, 1.9876, 2.9085, and 1.8492, respectively. With the increase of irradiation time, the UV-vis absorption peaks of the four organic dyes decreased. After 40 min simulated sunlight irradiation, the UV-vis absorbance of RhB, MB, CR, and MO decreased to 0.0426, 0.0592, 0.1975, and 0.3584, respectively, which proved that the organic dyes had been effectively degraded.

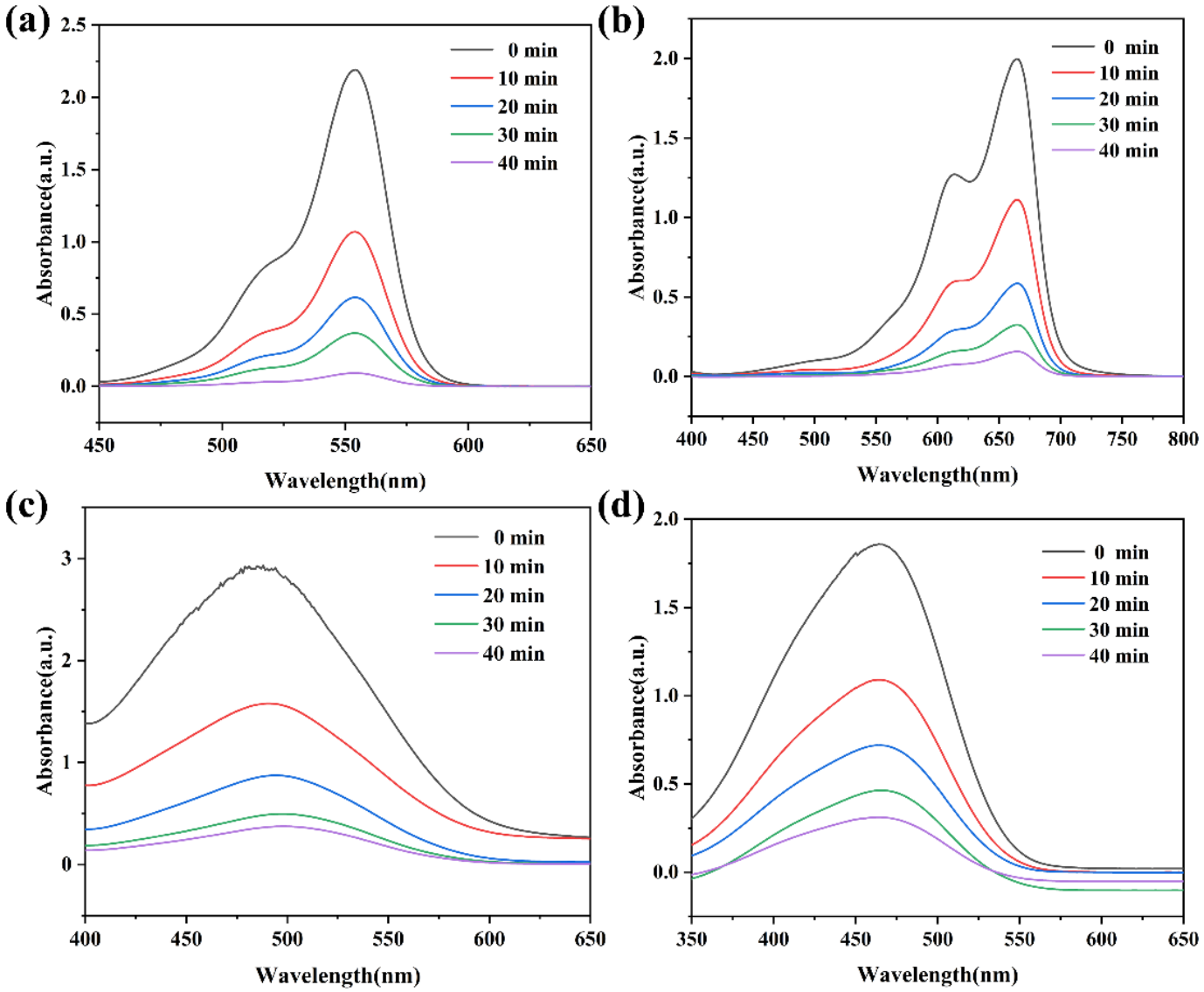

Figure 12. UV-vis absorbances of (**a**) RhB, (**b**) MB, (**c**) CR, and (**d**) MO with the variation in the irradiation time [Reaction conditions: initial concentration = 12 mg/L, photocatalyst = 0.2 g, solution pH of MO and CR: 2, solution pH of RhB and MB: 10, t = 40 min, simulated sunlight irradiation].

Figure 13 depicts the LC-MS analysis of RhB intermediates after photodegradation for 5 min, 10 min, 15 min, and 20 min. The *m/z* value determined the molecular weight of the intermediate product after photocatalytic degradation. It could be seen that after 5–20 min of photocatalytic degradation, the main peak of the *m/z* value of RhB dye decreased from 355.11 to 128.95. The RhB intermediates (*m/z* > 240) of larger molecular weight had been completely degraded into small molecules after 20 min of photocatalysis, which proved the occurrence of a photocatalytic redox reaction. It was concluded that the photocatalytic degradation process mainly involved the de-ethylation of RhB, the cracking and mineralization of chromophore [48].

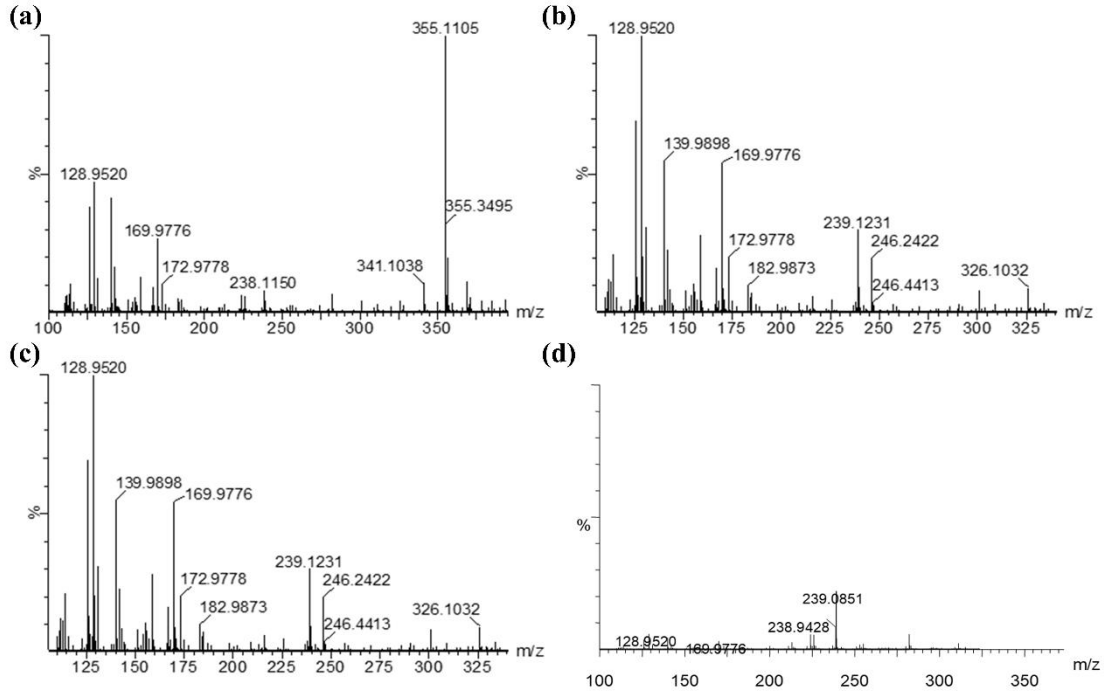

Figure 13. LC/MS spectra of RhB degradation with PAN/PANI–Sb_2S_3–ZnO after (**a**) 5 min, (**b**) 10 min, (**c**) 15 min, and (**d**) 20 min illumination.

2.5. The Photocatalytic Mechanism of PAN/PANI−Sb_2S_3−ZnO Membrane

The main active species produced by the PAN/PANI–Sb_2S_3–ZnO membrane during photocatalysis were investigated using free radical capture experiments, as shown in Figure 14a. $\bullet O_2^-$, •OH, h^+, and e^- were quenched by adding BQ, t-BuOH, OA, and $AgNO_3$, respectively [49–51]. It was observed that the photocatalytic degradation efficiency decreased after the addition of trapping agents. The dye removal efficiencies decreased to 45.64% and 52.9% after adding t-BuOH and BQ, which indicated that •OH and $\bullet O_2^-$ were the main reactive species in the photocatalytic process. After adding OA and $AgNO_3$, the photocatalytic degradation effects were reduced to 76.03% and 87.64%, respectively, indicating that h^+ and e^- played a supporting role in the photocatalytic reaction.

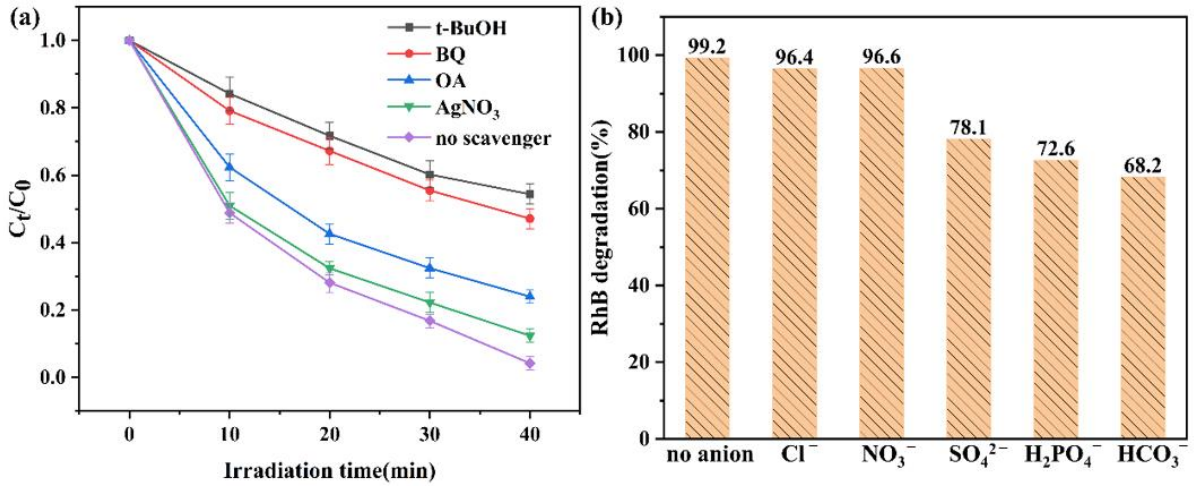

Figure 14. Degradation efficiency of PAN/PANI–Sb_2S_3–ZnO for RhB in the presence of (**a**) different scavengers and (**b**) different anions [Reaction conditions: initial concentration = 12 mg/L, photocatalyst = 0.2 g, pH value for RhB solutions = 10, t = 40 min, simulated sunlight irradiation].

The aqueous environment contained a variety of anions that had unpredictable effects on the photocatalytic activity. Thus, the influences of coexisting ions (NaCl (Cl^-), $NaNO_3$ (NO_3^-), Na_3PO_4 ($H_2PO_4^-$), Na_2SO_4 (SO_4^{2-}), and $NaHCO_3$ (HCO_3^-)), with a concentration of 30 mM in the PAN/PANI–Sb_2S_3–ZnO photocatalytic system, were evaluated. The dye degradation was slightly affected by Na^+ because of its inert nature [52]. As shown in Figure 14b, after the addition of Cl^- and NO_3^-, the degradation efficiency of RhB did not decrease significantly. When SO_4^{2-}, $H_2PO_4^-$, and HCO_3^- were added, the degradation efficiencies for RhB dye decreased to 78.1%, 72.6%, and 68.2%, respectively. According to the free radical trapping experiments, •OH and h^+ were active species in the photocatalytic reaction process. •OH or h^+ were consumed by SO_4^{2-}, $H_2PO_4^-$, and HCO_3^-, and produced $\bullet SO_4^-$, $\bullet H_2PO_4$, and $\bullet CO_3^-$, as shown in Equations (1)–(5). Although the generated $\bullet SO_4^-$, $\bullet H_2PO_4$, and $\bullet CO_3^-$ as active species could degrade organic dyes, their redox performance was lower than that of •OH and h^+ [53].

$$SO_4^{2-} + h^+ \rightarrow \bullet SO_4^- \quad (1)$$

$$SO_4^{2-} + \bullet OH \rightarrow \bullet SO_4^- + OH^- \quad (2)$$

$$HCO_3^- + \bullet OH \rightarrow \bullet CO_3^- + H_2O \quad (3)$$

$$H_2PO_4^- + h^+ \rightarrow \bullet H_2PO_4 \quad (4)$$

$$H_2PO_4^- + \bullet OH \rightarrow \bullet H_2PO_4 + OH^- \quad (5)$$

To better understand the heterojunction structure, Tauc plots and Mott–Schottky tests were conducted, as shown in Figure 15. The band gap energy was calculated using Equation (6):

$$(\alpha h\nu) = C\left(h\nu - E_g\right)^n \quad (6)$$

where α is the light absorption coefficient, $h\nu$ represents the incident photon energy, E_g is the band gap energy, and C is the light speed. The calculated E_g for PANI, Sb_2S_3, and ZnO was 2.80, 1.75, and 3.15 eV, respectively. The Mott–Schottky plots of PANI, Sb_2S_3, and ZnO are shown in Figure 16d–f. The flat band potential values (E_{fb}) of PANI, Sb_2S_3, and ZnO acquired from the x-intercept in Mott–Schottky plots were approximately 0.43, −0.72, and −0.47 (vs. Ag/AgCl reference). The normal hydrogen electrode potential (E_{NHE}) could be calculated with Equation (7):

$$E_{NHE} = E_{Ag/AgCl} + 0.197 \quad (7)$$

The highest occupied molecular orbital (HOMO) potential of PANI was equal to its standard hydrogen electrode potential, while the conduction band (CB) potential of Sb_2S_3 and ZnO was equal to the standard hydrogen electrode potential. Thus, the HOMO potential of PANI was 0.63 eV, and the CB potential of Sb_2S_3 and ZnO was −0.52 eV and −0.27 eV. According to Equation (8), the lowest unoccupied molecular orbital (LUMO) potential of PANI was −2.17 eV, and the valence band (VB) potential of Sb_2S_3 and ZnO was 1.23 eV and 2.88 eV, respectively.

$$E_{VB/HOMO} = E_{CB/LUMO} + E_g \quad (8)$$

Based on the above discussion, two possible photocatalytic mechanisms were proposed. It was assumed that the composite photocatalyst conformed to the e^-h^+ migration mechanism of the traditional type II heterojunction, as shown in Figure 16a. Under simulated sunlight irradiation, the electrons in PANI, Sb_2S_3, and ZnO absorbed light energy and produced photogenerated e^-–h^+. The e^- in the CB of PANI and Sb_2S_3 would migrate

to the CB of ZnO, while h^+ in the VB of Sb_2S_3 and ZnO would migrate to the VB of PANI; thus, the separation efficiency of e^-–h^+ was promoted. However, the electrons and holes accumulated in the CB of ZnO and VB of PANI both reduced the generation of reactive oxygen species ($\bullet O_2^-$ and •OH). At the same time, the CB position (−0.27 eV) was lower than the standard redox potential of $O_2/\bullet O_2^-$ (−0.33 eV), so the electrons accumulated in the CB of ZnO could not reduce O_2 to form $\bullet O_2^-$. Moreover, the addition of TEMPOL ($\bullet O_2^-$ scavenger) did not affect the degradation rate of RhB with pure ZnO (Figure S2), which further indicated that $\bullet O_2^-$ did not play a role in the degradation of RhB by ZnO. 5,5-dimethyl-1-pyrrolineN-oxide (DMPO) was used as the spin trap to detect the $\bullet O_2^-$ produced under light using electron spin resonance (ESR), which further verified that ZnO could not generate $\bullet O_2^-$. As shown in Figure S3, the signal of DMPO-$\bullet O_2^-$ was not observed in the systems with the photocatalysts of ZnO with light illumination, suggesting that no $\bullet O_2^-$ radicals were generated. In addition, the HOMO of PANI (0.63 eV) was lower than the standard redox potential of $H_2O/\bullet OH$ (2.7 eV) and $OH^-/\bullet OH$ (1.99 eV), so h^+ in PANI could not react with H_2O or OH^- to form •OH. Therefore, according to the traditional type II heterojunction mechanism, e^- and h^+ were the main photocatalytic active species, which was inconsistent with the results of the free radical trapping experiments.

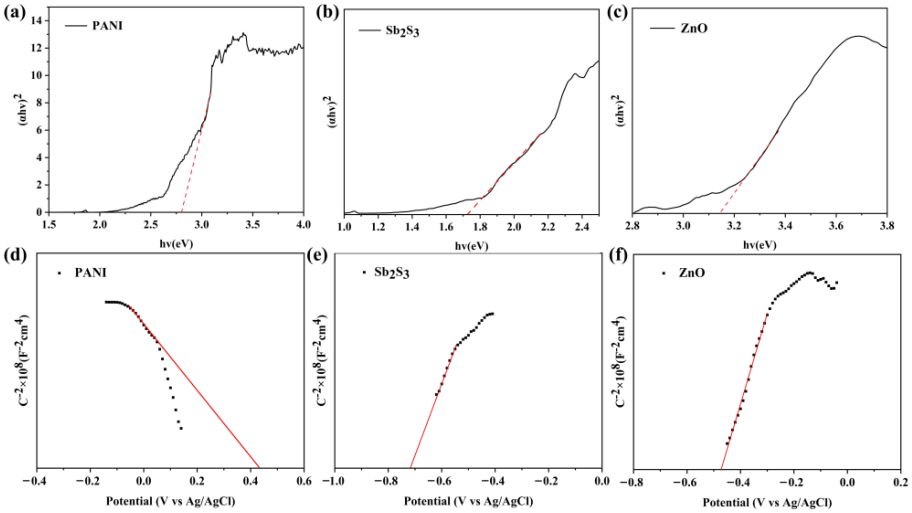

Figure 15. Tauc plots of (**a**) PANI, (**b**) Sb_2S_3, and (**c**) ZnO. Mott–Schottky plots of (**d**) PANI, (**e**) Sb_2S_3, and (**f**) ZnO.

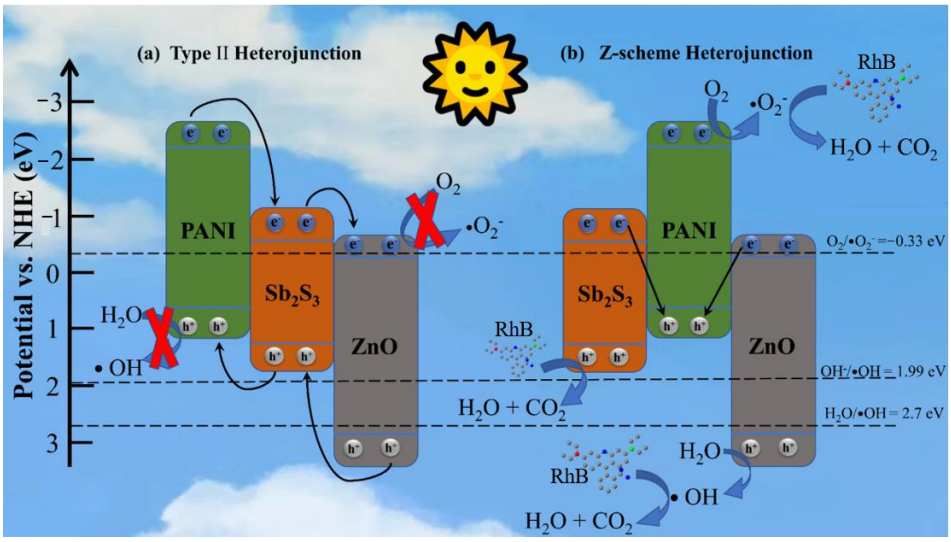

Figure 16. Schematic diagram of the organic dye removal mechanism. (**a**) traditional type-II heterojunction and (**b**) Z-scheme heterojunction charge transfer pathway.

Figure 16b shows the dual Z-type heterojunction mechanism of the composite photocatalyst. The e^- of Sb_2S_3 and ZnO would migrate to the VB of PANI and recombine with the h^+ in PANI; thus, h^+ in the VB of Sb_2S_3/ZnO and e^- in the CB of PANI could be preserved. The LUMO position of PANI was higher than the standard redox potential of $O_2/\bullet O_2^-$ (–0.33 eV), and e^- in the LUMO of PANI could react with O_2 to form $\bullet O_2^-$. The VB position of ZnO (2.88 eV) was higher than the standard redox potential of $H_2O/\bullet OH$ (2.7 eV) and $OH^-/\bullet OH$ (1.99 eV), so h^+ in the VB of ZnO could react with H_2O or OH^- to produce •OH. •OH and $\bullet O_2^-$ were the main photocatalytic reactive species in the assumed dual Z-type heterojunction mechanism, which in agreement with the conclusion of the free radical trapping experiment.

2.6. Reusability and Stability of PAN/PANI–Sb_2S_3–ZnO

The degradation efficiency after recycling the photodegradation experiments five times is shown in Figure 17a. It could be seen that the degradation efficiency for RhB dye was only slightly reduced, indicating that the photocatalyst had great reusability. Figure 18b shows the FTIR of the PAN/PANI–Sb_2S_3–ZnO membrane before and after recycling the photodegradation experiments five times. It was observed that the FTIR peak had not significantly changed before and after the degradation reaction, indicating that PAN/PANI–Sb_2S_3–ZnO had good stability.

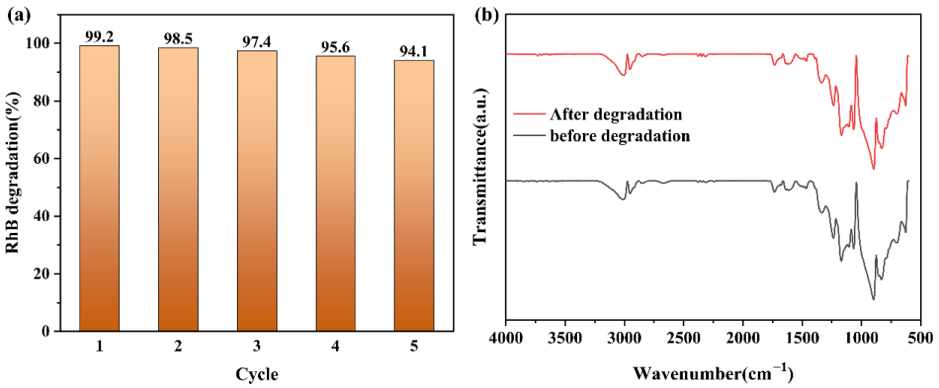

Figure 17. (**a**) Cyclic degradation efficiency of RhB and (**b**) FTIR before and after degradation of PAN/PANI–Sb_2S_3–ZnO composite film.

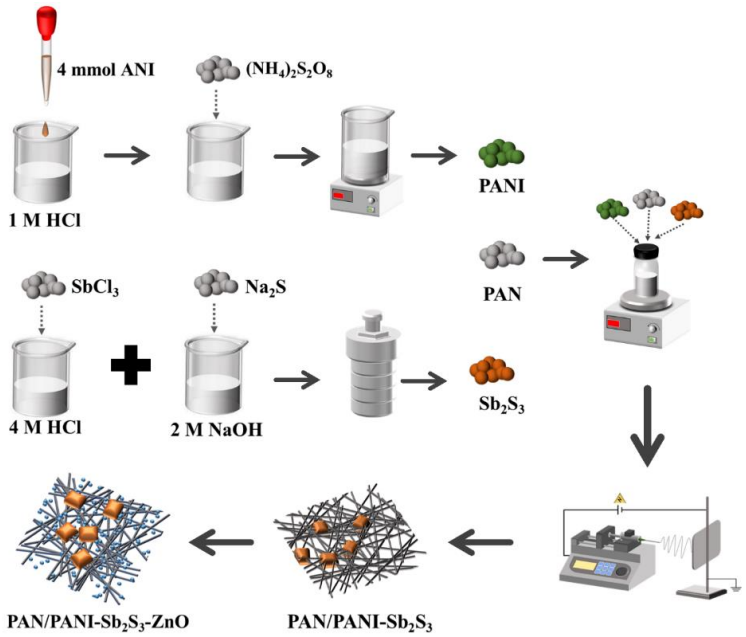

Figure 18. Schematic illustration of the preparation of composite membranes.

3. Experimental

3.1. Materials

Aniline (ANI), ammonium persulfate ($(NH_4)_2S_2O_8$), ZnO, Rhodamine B (RhB) (99%), methylene blue (MB) (99%), Congo red (CR) (99%), methyl orange (MO) (99%), $SbCl_3$, and $Na_2S{\bullet}9H_2O$ were all purchased from Aladdin Industrial Corporation, Shanghai, China. Sodium hydroxide (NaOH), hydrochloric acid (HCl, 36~38%), N, N-dimethylformamide (DMF), polyacrylonitrile (PAN, Mw = 150,000 g/mol), and ethyl alcohol were obtained from Beijing Chemical Works. Benzoquinone (BQ), oxalic acid (OA), and tert-Butanol (t-BuOH) were ordered from Sinopharm Chemical Reagent Co. LTD (Shanghai, China). Deionized (DI) water was obtained from the laboratory. All of these chemicals were of analytical grade and utilized without further purification.

3.2. The Preparation of Composite Membranes

3.2.1. The Preparation of PANI

First, 4 mmol ANI was added drop by drop into 200 mL 1 M HCl solution and stirred for 1 h as solution A. Then, 4 mmol $(NH_4)_2S_2O_8$ was dissolved in 200 mL 1 M HCl and stirred for 1 h as solution B. Solution B was slowly added to solution A and stirred at 0 °C in ice bath for 12 h. Finally, the prepared PANI was washed with anhydrous ethanol and deionized water, and dried in oven at 60 °C.

3.2.2. The Preparation of Sb_2S_3

A total of 1.52 g $SbCl_3$ was dissolved in 50 mL solution of 4 M HCl and 2.4 g Na_2S was dissolved in 100 mL solution of 2 M NaOH. After stirring at room temperature for 30 min, $SbCl_3$/HCl solution was slowly added into Na_2S/NaOH solution, and stirring continued for 1 h. Then, the suspension was heated at 100 °C in a 200 mL Teflon-lined autoclave for 12 h. At room temperature, the obtained Sb_2S_3 was separated using filtration, washed with deionized water, and dried at 60 °C for 6 h.

3.2.3. The Preparation of PAN/PANI-Sb_2S_3 Fiber Membrane

PAN was selected to improve spinnability of PANI in this experiment. A total of 1 g PAN and 0.2 g PANI were dissolved in 10 mL DMF and stirred at room temperature for 12 h to obtain PAN/PANI electrospinning precursor solution. Then, 2% *w/v* Sb_2S_3 was added into PAN/PANI solution. The PAN/PANI-Sb_2S_3 precursor solution was obtained through stirring for 12 h. Before electrospinning, the precursor solution was ultrasonically treated for 1 h.

A 5 mL plastic syringe with an inner diameter of 0.6 mm was used as the spinneret and 10 cm × 10 cm aluminum foil was used as the receiver in the electrospinning process. Electrospinning was performed at a voltage of 16 kV, the distance between the syringe tip and the receiver was 15 cm, and the feeding rate was set to 1 mL/h. During the experiment, the ambient temperature was 20 ± 2 °C and the relative humidity was 10–20%.

3.2.4. The Preparation of PAN/PANI–Sb_2S_3–ZnO Membrane

To obtain the well-dispersed ZnO in PAN/PANI-Sb_2S_3, the surface ultrasonic method was used to prepare the PAN/PANI–Sb_2S_3–ZnO membrane. The PAN/PANI-Sb_2S_3 fiber membrane was immersed in the ZnO suspension (0.5% *w/v*) and ultrasound treatment for 1 h. The preparation process is shown in Figure 1.

3.3. Characterizations

The membranes' morphologies were observed using FE-SEM (JSM-6700 F, JEOL, Shimadzu Corporation, Kyoto, Japan). TEM (JEM-2100 F, JEOL, Kyoto Japan) was used to detected the internal structures and elements distribution of the membranes. The component structures of membranes were characterized using Fourier transform infrared spectroscopy (FTIR-4100, JASCO, Kyoto, Japan) in the wave number range of 400–4000 cm^{-1}. The crystal structure was analyzed using a Siemens D5000 X-ray diffractometer (XRD) using

copper target Kα ray, 40 mA current, 40 kV voltage, and 4° min^{-1} scan speed (Shanghai Metash Instrument Co. Ltd., Shanghai, China). The surface chemical components of the membranes were examined using an X-ray photoelectron spectroscope (XPS, ESCALab220i-XL VG Science, Walser M, MA, USA). The absorption performance for dye solutions of the samples was evaluated using UV-vis spectroscopy (UV-6100S, MAPADA, Shanghai Metash Instrument Co. Ltd., Shanghai, China). The electron spin resonance (ESR) spectra data were obtained using a Bruker EPR A 300-10/12 spectrometer for tracing the active species. The pH values of dyes were adjusted in the range of 2.0–8.0 using HCl or NaOH. Pen-type pH meter (pH8180-0-00, Hong Kong Xima Instrument Technology Co. Ltd., Shanghai, China) was used to measure the pH value of dye solutions. The surface zeta potential of the membranes was determined using zeta potential analyzer (NanoZS90, London, UK). UV-vis diffuse reflectance spectroscopy (UV-vis DRS) was obtained on a Cary 500 spectrometer. The electrochemical properties of the membranes were investigated using electrochemical workstations (CHI660D, Beijing Merry Change Technology Co. Ltd., Beijing, China). The composite membranes, Pt nod, and Ag/AgCl electrode were used as the working, counter, and reference electrodes, respectively. The photoluminescence (PL) spectra and time-resolved photoluminescence spectra (TRPS) were measured with an Edinburgh FLS 980 apparatus at an excitation wavelength of 253 nm (Shimadzu, Kyoto, Japan). A xenon lamp source (PLS-SXE300+/300UV) with a spectral range of 320–780 nm was used to simulate sunlight (Beijing Merry Change Technology Co. Ltd., Beijing, China). Chromatographic separation of the aliquots was performed using an Agilent 1290 infinity LC (Agilent Technologies, Bellevue, WA, USA), an Agilent Eclipse Plus C18 column (2.1 mm × 50 mm, 1.8 μm), and a mobile phase composed of 0.1% FA in water (A) and 0.1% FA in ACN (B). The flow rate was 0.3 mL/min, and the injection volume was 1 μL, which was injected into the column using a thermostated HiP-ALS autosampler. For profiling and identification of by-products formed during the photocatalytic process, the separated peaks were analyzed using an Agilent 6550 QTOF (Agilent Technologies, Beijing, China) providing high-resolution mass measurement.

3.4. Photocatalytic Degradation of Dyes

A total of 12 mg of dyes (RhB, MB, CR, MO) was dissolved in 1 L of distilled water to obtain 12 mg/L dye concentration. The prepared fiber membrane (0.2 g) was immersed in 60 mL organic dye solution (12 mg L^{-1}) under dark condition for 30 min. Then, the entire experimental setup was irradiated under visible light source for 60 min, and the light intensity was approximately 20 mW $(cm^2)^{-1}$. The pH of dyes was adjusted using HCl or NaOH. A UV-vis spectrophotometer was used to measure the concentrations of organic dye solutions before and after degradation. The removal rate (R%) was calculated using the following Equation (9):

$$R(\%) = \frac{C_0 - C_t}{C_0} \times 100\% \quad (9)$$

where C_0 (mg L^{-1}) and C_t (mg L^{-1}) represent the initial and equilibrium concentration of organic dyes, respectively.

3.5. Kinetic Model Analysis

The nonlinear kinetic model of pseudo-first order (Equation (10)) was fitted to experimental data.

$$\frac{C_0}{C} = e^{-k_{app}t} \quad (10)$$

where C_0 is the dyes' initial concentration, C is the dyes' concentration at the time t (min), and k_{app} is the apparent first-order rate constant. From k_{app} the half-life time ($t_{1/2}$) was obtained using Equation (11), as follows:

$$t_{1/2} = \frac{ln2}{k_{app}} \quad (11)$$

4. Conclusions

In this work, the novel dual Z-scheme organic/inorganic PAN/PANI–Sb_2S_3–ZnO photocatalyst was designed using electrospinning and surface ultrasound. PAN/PANI–Sb_2S_3–ZnO exhibited a wide spectral absorption range from ultraviolet to visible light. Under 40 min irradiation, the PAN/PANI–Sb_2S_3–ZnO membrane almost achieved complete degradation for RhB, MB, MO, and CR dyes. The photocatalytic mechanism showed that PANI, Sb_2S_3, and ZnO formed a dual Z-type heterostructure, which not only achieved efficient carrier separation, but also retained photogenerated e^- and h^+ with strong redox capacity. It was also verified that •OH and $\bullet O_2^-$ were the main active species during the photocatalytic reaction. In addition, the PAN/PANI–Sb_2S_3–ZnO composite membrane also had high stability and reusability. This work provided a research strategy for constructing novel dual organic/inorganic photocatalysts with designable heterojunction structures.

Supplementary Materials: The following supporting information can be downloaded at: https://www.mdpi.com/article/10.3390/catal13111391/s1, Figure S1: Corresponding reaction rate diagram of RhB with different initial concentrations by PAN/PANI-Sb_2S_3-ZnO, Figure S2: The degradation of RhB by ZnO with or without TEMPOL. [Experimental conditions: Initial concentration = 12 mg/L, photocatalyst = 0.2 g, TEMPOL concentration = 10 Mm, pH value for RhB solutions = 10, t = 40 min, UV light irradiation, Figure S3: ESR spectra of radical adducts trapped by DMPO in ZnO for superoxide radical, Table S1: The pseudo-first order kinetic model kinetic parameters of RhB photocatalytic experiments, Table S2: The pseudo-first order kinetic model kinetic parameters of RhB, MB, CR and MO photocatalytic experiments by PAN/PANI-Sb_2S_3-ZnO, Table S3: Comparison of degradation rate of PAN/PANI-Sb_2S_3-ZnO with other photocatalysts toward RhB and MB, Table S4: L-H model kinetic parameters for different initial concentrations of RhB by PAN/PANI-Sb_2S_3-ZnO. References [54–59] are cited in the Supplementary Materials.

Author Contributions: T.Y.: data analysis and writing. D.W.: conceptualization, methodology, formal analysis, validation, data curation, and writing—original draft. L.L.: validation, resources, writing—review and editing, visualization, supervision, project administration, and funding acquisition. W.S.: data curation and visualization. C.L.: validation, resources, writing—review and editing, and visualization. X.P.: validation, resources, and writing—review and editing. All authors have read and agreed to the published version of the manuscript.

Funding: This research was supported by the Science and Technology Development Plan of Jilin Province (20230201152GX).

Data Availability Statement: All research data are included in this article.

Conflicts of Interest: The authors declare no conflict of interests.

References

1. Zhou, L.; Xiao, G.Q.; He, Y.; Wu, J.C.; Shi, H.; Yin, X.Y.; He, T.; Li, Z.Y.; Chen, J.Y. Multi-Functional Composite Membrane with Strong Photocatalysis to Effectively Separate Emulsified-Oil/Dyes from Complex Oily Sewage. *Colloids Surf. A-Physicochem. Eng. Asp.* **2022**, *643*, 13. [CrossRef]
2. Du, F.Q.; Yang, D.M.; Kang, T.X.; Ren, Y.X.; Hu, P.; Song, J.M.; Teng, F.; Fan, H.B. SiO_2/Ga_2O_3 Nanocomposite for Highly Efficient Selective Removal of Cationic Organic Pollutant Via Synergistic Electrostatic Adsorption and Photocatalysis. *Sep. Purif. Technol.* **2022**, *295*, 10. [CrossRef]
3. Cionti, C.; Pargoletti, E.; Falletta, E.; Bianchi, C.L.; Meroni, D.; Cappelletti, G. Combining Ph-Triggered Adsorption and Photocatalysis for the Remediation of Complex Water Matrices. *J. Environ. Chem. Eng.* **2022**, *10*, 9. [CrossRef]
4. Huang, X.F.; Xu, X.Y.; Yang, R.Y.; Fu, X.H. Synergetic adsorption and photocatalysis performance of g-C3N4/Ce-doped MgAl-LDH in degradation of organic dye under LED visible light. *Colloid Surf. A-Physicochem. Eng. Asp.* **2022**, *643*, 13. [CrossRef]
5. Lan, F.; Liu, C.S.; Zhou, C.; Huang, X.Z.; Wu, J.Y.; Zhang, X. Developing highly reducing conjugated porous polymer: A metal-free and recyclable approach with superior performance for pinacol C-C coupling under visible light. *J. Mater. Chem. A* **2022**, *10*, 16578–16584. [CrossRef]
6. Yuan, X.J.; Remita, H. Conjugated Polymer Polypyrrole Nanostructures: Synthesis and Photocatalytic Applications. *Top. Curr. Chem.* **2022**, *380*, 34. [CrossRef] [PubMed]
7. Wu, B.; Liu, Y.; Zhang, Y.X.; Fan, L.; Li, Q.Y.; Yu, Z.Y.; Zhao, X.S.; Zheng, Y.C.; Wang, X.J. Molecular engineering of covalent triazine frameworks for highly enhanced photocatalytic aerobic oxidation of sulfides. *J. Mater. Chem. A* **2022**, *10*, 12489–12496. [CrossRef]

8. Li, Z.L.; Fang, H.; Chen, Z.P.; Zou, W.X.; Zhao, C.X.; Yang, X.F. Regulating donor-acceptor interactions in triazine-based conjugated polymers for boosted photocatalytic hydrogen production. *Appl. Catal. B-Environ.* **2022**, *312*, 9. [CrossRef]
9. Kumar, H.; Luthra, M.; Punia, M.; Singh, D. Ag2O@PANI nanocomposites for advanced functional applications: A sustainable experimental and theoretical approach. *Colloid Surf. A-Physicochem. Eng. Asp.* **2022**, *640*, 12. [CrossRef]
10. Celebi, N.; Soysal, F.; Salimi, K. Dual-functional PANI/MIL-125(Ti) photoanodes for enhanced photoelectrochemical H-2 generation and photothermal heating. *Mater. Chem. Phys.* **2022**, *291*, 9. [CrossRef]
11. Lin, A.J.; Ren, M.; Tan, X.; Ma, J.; Zhang, Y.; Yang, T.X.; Pei, Y.S.; Cui, J. Visible-light-driven melamine foam/PANI/N,O,P containing covalent organic polymer for achieving H_2O_2 production and boosting Fe(II)/Fe(III) cycle. *J. Clean. Prod.* **2022**, *345*, 12. [CrossRef]
12. Sboui, M.; Niu, W.K.; Li, D.Z.; Lu, G.; Zhou, N.; Zhang, K.; Pan, J.H. Fabrication of electrically conductive TiO_2/PANI/PVDF composite membranes for simultaneous photoelectrocatalysis and microfiltration of azo dye from wastewater. *Appl. Catal. A-Gen.* **2022**, *644*, 10. [CrossRef]
13. Xu, D.; Huang, Y.; Ma, Q.; Qiao, J.Z.; Guo, X.; Wu, Y.Q. A 3D porous structured cellulose nanofibrils-based hydrogel with carbon dots-enhanced synergetic effects of adsorption and photocatalysis for effective Cr(VI) removal. *Chem. Eng. J.* **2023**, *456*, 11. [CrossRef]
14. Wang, F.; Xu, J.; Wang, Z.P.; Lou, Y.; Pan, C.S.; Zhu, Y.F. Unprecedentedly efficient mineralization performance of photocatalysis-self-Fenton system towards organic pollutants over oxygen-doped porous g-C_3N_4 nanosheets. *Appl. Catal. B-Environ.* **2022**, *312*, 9. [CrossRef]
15. Chen, Q.S.; Zhou, H.Q.; Wang, J.C.; Bi, J.H.; Dong, F. Activating earth-abundant insulator $BaSO_4$ for visible-light induced degradation of tetracycline. *Appl. Catal. B-Environ.* **2022**, *307*, 12. [CrossRef]
16. Xia, L.H.; Sun, Z.L.; Wu, Y.N.; Yu, X.F.; Cheng, J.B.; Zhang, K.S.; Sarina, S.; Zhu, H.Y.; Weerathunga, H.; Zhang, L.X.; et al. Leveraging doping and defect engineering to modulate exciton dissociation in graphitic carbon nitride for photocatalytic elimination of marine oil spill. *Chem. Eng. J.* **2022**, *439*, 15. [CrossRef]
17. Feng, Z.Y.; Zhu, X.W.; Yang, J.M.; Zhong, K.; Jiang, Z.F.; Yu, Q.; Song, Y.H.; Hua, Y.J.; Li, H.M.; Xu, H. Inherent Facet-Dominant effect for cobalt oxide nanosheets to enhance photocatalytic CO_2 reduction. *Appl. Surf. Sci.* **2022**, *578*, 9. [CrossRef]
18. Chen, Y.N.; Yang, L.; Sun, Y.N.; Guan, R.Q.; Liu, D.; Zhao, J.; Shang, Q.K. A high-performance composite CDs@Cu-HQCA/TiO_2 flower photocatalyst: Synergy of complex-sensitization, TiO_2-morphology control and carbon dot-surface modification. *Chem. Eng. J.* **2022**, *436*, 17. [CrossRef]
19. Zhang, Y.T.; Zhang, T.; Jia, J.; Lin, G.; Li, K.K.; Zheng, L.S.; Li, X.; Kong, Z.H. Construction of $Zn_{0.2}Cd_{0.8}S$/g-C_3N_4 nanosheet array heterojunctions toward enhanced photocatalytic reduction of CO_2 in visible light. *Colloid Surf. A-Physicochem. Eng. Asp.* **2022**, *655*, 10. [CrossRef]
20. Peng, Q.; Tang, X.K.; Liu, K.; Zhong, W.L.; Zhang, Y.J.; Xing, J.J. Synthesis of silica nanofibers-supported BiOCl/TiO_2 heterojunction composites with enhanced visible-light photocatalytic performance. *Colloid Surf. A-Physicochem. Eng. Asp.* **2022**, *652*, 11. [CrossRef]
21. Yang, H.; Hao, H.S.; Zhao, Y.R.; Hu, Y.T.; Min, J.K.; Zhang, G.L.; Bi, J.R.; Yan, S.; Hou, H.M. An efficient construction method of S-scheme Ag2CrO4/ZnFe2O4 nanofibers heterojunction toward enhanced photocatalytic and antibacterial activity. *Colloid Surf. A-Physicochem. Eng. Asp.* **2022**, *641*, 10. [CrossRef]
22. Xu, F.; Chai, B.; Liu, Y.Y.; Liu, Y.L.; Fan, G.Z.; Song, G.S. Superior photo-Fenton activity toward tetracycline degradation by 2D?-Fe_2O_3 anchored on 2D g-C3N4: S-scheme heterojunction mechanism and accelerated Fe^{3+}/Fe^{2+} cycle. *Colloid Surf. A-Physicochem. Eng. Asp.* **2022**, *652*, 14. [CrossRef]
23. Ge, L.; Han, C.C.; Liu, J. In situ synthesis and enhanced visible light photocatalytic activities of novel PANI-g-C_3N_4 composite photocatalysts. *J. Mater. Chem.* **2012**, *22*, 11843–11850. [CrossRef]
24. Wang, Q.Z.; Hui, J.; Li, J.J.; Cai, Y.X.; Yin, S.Q.; Wang, F.P.; Su, B.T. Photodegradation of methyl orange with PANI-modified BiOCl photocatalyst under visible light irradiation. *Appl. Surf. Sci.* **2013**, *283*, 577–583. [CrossRef]
25. Chen, Y.Q.; Cheng, Y.F.; Zhao, J.F.; Zhang, W.W.; Gao, J.H.; Miao, H.; Hu, X.Y. Construction of Sb_2S_3/CdS/$CdIn_2S_4$ cascaded S-scheme heterojunction for improving photoelectrochemical performance. *J. Colloid Interface Sci.* **2022**, *627*, 1047–1060. [CrossRef] [PubMed]
26. Wang, F.; Yang, C.L.; Wang, M.S.; Ma, X.G. Photocatalytic hydrogen evolution reaction with high solar-to-hydrogen efficiency driven by the Sb_2S_3 monolayer and RuI2/Sb_2S_3 heterostructure with solar light. *J. Power Sources* **2022**, *532*, 10. [CrossRef]
27. Cheng, Y.F.; Gong, M.; Xu, T.T.; Liu, E.Z.; Fan, J.; Miao, H.; Hu, X.Y. Epitaxial Grown Sb_2Se_3@Sb_2S_3 Core-Shell Nanorod Radial-Axial Hierarchical Heterostructure with Enhanced Photoelectrochemical Water Splitting Performance. *ACS Appl. Mater. Interfaces* **2022**, *14*, 23785–23796. [CrossRef]
28. Xu, W.; Xu, L.H.; Pan, H.; Wang, L.M.; Shen, Y. Superamphiphobic cotton fabric with photocatalysis and ultraviolet shielding property based on hierarchical ZnO/halloysite nanotubes hybrid particles. *Colloid Surf. A-Physicochem. Eng. Asp.* **2022**, *654*, 11. [CrossRef]
29. Meenakshi, G.; Sivasamy, A. Enhanced photocatalytic activities of CeO_2@ZnO core-shell nanostar particles through delayed electron hole recombination process. *Colloid Surf. A-Physicochem. Eng. Asp.* **2022**, *645*, 13. [CrossRef]
30. Ramos, P.G.; Sanchez, L.A.; Rodriguez, J.M. A review on improving the efficiency of photocatalytic water decontamination using ZnO nanorods. *J. Sol-Gel Sci. Technol.* **2022**, *102*, 105–124. [CrossRef]

31. Gao, Y.; Yan, N.; Jiang, C.; Xu, C.; Yu, S.; Liang, P.; Zhang, X.; Liang, S.; Huang, X. Filtration-enhanced highly efficient photocatalytic degradation with a novel electrospun rGO@TiO_2 nanofibrous membrane: Implication for improving photocatalytic efficiency. *Appl. Catal. B Environ.* **2020**, *268*, 118737. [CrossRef]
32. Selvinsimpson, S.; Gnanamozhi, P.; Pandiyan, V.; Govindasamy, M.; Habila, M.A.; AlMasoud, N.; Chen, Y. Synergetic effect of Sn doped ZnO nanoparticles synthesized via ultrasonication technique and its photocatalytic and antibacterial activity. *Environ. Res.* **2021**, *197*, 111115. [CrossRef] [PubMed]
33. Qu, C.; Zhao, P.; Wu, C.D.; Zhuang, Y.; Liu, J.M.; Li, W.H.; Liu, Z.; Liu, J.H. Electrospun PAN/PANI fiber film with abundant active sites for ultrasensitive trimethylamine detection. *Sens. Actuator B-Chem.* **2021**, *338*, 9. [CrossRef]
34. Dashairya, L.; Sharma, M.; Basu, S.; Saha, P. Enhanced dye degradation using hydrothermally synthesized nanostructured Sb_2S_3/rGO under visible light irradiation. *J. Alloys Compd.* **2018**, *735*, 234–245. [CrossRef]
35. Lopez-Lopez, J.; Tejeda-Ochoa, A.; Lopez-Beltran, A.; Herrera-Ramirez, J.; Mendez-Herrera, P. Sunlight Photocatalytic Performance of ZnO Nanoparticles Synthesized by Green Chemistry Using Different Botanical Extracts and Zinc Acetate as a Precursor. *Molecules* **2022**, *27*, 17. [CrossRef] [PubMed]
36. Wang, S.; Zhao, Y.; Zhang, M.Y.; Feng, J.; Wei, T.; Ren, Y.M.; Ma, J. Electrostatic self-assembled layered polymers form supramolecular heterojunction catalyst for photocatalytic reduction of high-stability nitrate in water. *J. Colloid Interface Sci.* **2022**, *622*, 828–839. [CrossRef]
37. Hosny, M.; Fawzy, M.; Eltaweil, A.S. Green synthesis of bimetallic Ag/ZnO@Biohar nanocomposite for photocatalytic degradation of tetracycline, antibacterial and antioxidant activities. *Sci. Rep.* **2022**, *12*, 17. [CrossRef]
38. Zhang, H.L.; Hu, C.G.; Ding, Y.; Lin, Y. Synthesis of 1D Sb_2S_3 nanostructures and its application in visible-light-driven photodegradation for MO. *J. Alloys Compd.* **2015**, *625*, 90–94. [CrossRef]
39. Yasin, M.; Saeed, M.; Muneer, M.; Usman, M.; ul Haq, A.; Sadia, M.; Altaf, M. Development of Bi_2O_3-ZnO heterostructure for enhanced photodegradation of rhodamine B and reactive yellow dyes. *Surf. Interfaces* **2022**, *30*, 12. [CrossRef]
40. Wang, C.; Wang, L.; Jin, J.; Liu, J.; Li, Y.; Wu, M.; Chen, L.H.; Wang, B.J.; Yang, X.Y.; Su, B.L. Probing effective photocorrosion inhibition and highly improved photocatalytic hydrogen production on monodisperse PANI@CdS core-shell nanospheres. *Appl. Catal. B-Environ.* **2016**, *188*, 351–359. [CrossRef]
41. Li, F.; Zhang, L.L.; Hu, C.; Xing, X.C.; Yan, B.; Gao, Y.W.; Zhou, L. Enhanced azo dye decolorization through charge transmission by sigma-Sb3+-azo complexes on amorphous Sb_2S_3 under visible light irradiation. *Appl. Catal. B-Environ.* **2019**, *240*, 132–140. [CrossRef]
42. Sun, J.X.; Yuan, Y.P.; Qiu, L.G.; Jiang, X.; Xie, A.J.; Shen, Y.H.; Zhu, J.F. Fabrication of composite photocatalyst g-C_3N_4-ZnO and enhancement of photocatalytic activity under visible light. *Dalton Trans.* **2012**, *41*, 6756–6763. [CrossRef] [PubMed]
43. Wang, X.; Zhu, J.Q.; Yu, X.; Fu, X.H.; Zhu, Y.; Zhang, Y.M. Enhanced removal of organic pollutant by separable and recyclable rGH-PANI/BiOI photocatalyst via the synergism of adsorption and photocatalytic degradation under visible light. *J. Mater. Sci. Technol.* **2021**, *77*, 19–27. [CrossRef]
44. Dou, W.Y.; Hu, X.Y.; Kong, L.H.; Peng, X.J. Photo-induced dissolution of Bi2O3 during photocatalysis reactions: Mechanisms and inhibition method. *J. Hazard. Mater.* **2021**, *412*, 10. [CrossRef] [PubMed]
45. Liu, T.T.; Wang, Z.; Wang, X.R.; Yang, G.H.; Liu, Y. Adsorption-photocatalysis performance of polyaniline/dicarboxyl acid cellulose@graphene oxide for dye removal. *Int. J. Biol. Macromol.* **2021**, *182*, 492–501. [CrossRef]
46. Mallappa, M.; Nagaraju, K.; Shivaraj, Y. Enhanced Photocatalytic degradation of methylene blue dye using CuS-CdS nanocomposite under visible light irradiation. *Appl. Surf. Sci.* **2019**, *475*, 828–838. [CrossRef]
47. Dogar, S.; Nayab, S.; Farooq, M.Q.; Said, A.; Kamran, R.; Duran, H.; Yameen, B. Utilization of Biomass Fly Ash for Improving Quality of Organic Dye-Contaminated Water. *ACS Omega* **2020**, *5*, 15850–15864. [CrossRef]
48. Liang, C.; Cui, M.Y.; Zhao, W.; Dong, L.Y.; Ma, S.S.; Liu, X.T.; Wang, D.K.; Jiang, Z.J.; Wang, F. Hybridizing electron-mediated H5PMo10V2O40 with CdS/g-C3N4 for efficient photocatalytic performance of Z-scheme heterojunction in wastewater treatment. *Chemosphere* **2022**, *305*, 12. [CrossRef]
49. Wen, Y.; Wang, Z.W.; Cai, Y.H.; Song, M.X.; Qi, K.M.; Xie, X.Y. S-scheme BiVO4/CQDs/beta-FeOOH photocatalyst for efficient degradation of ofloxacin: Reactive oxygen species transformation mechanism insight. *Chemosphere* **2022**, *295*, 13. [CrossRef]
50. Zhou, X.Y.; Wang, T.Y.; Zhang, L.; Che, S.Y.; Liu, H.; Liu, S.X.; Wang, C.Y.; Su, D.W.; Teng, Z.Y. Highly efficient Ag_2O/Na-g-C_3N_4 heterojunction for photocatalytic desulfurization of thiophene in fuel under ambient air conditions. *Appl. Catal. B-Environ.* **2022**, *316*, 13. [CrossRef]
51. Ma, L.J.; Wu, H.Q.; Chen, B.Y.; Wang, G.; Lei, B.X.; Zhang, D.; Kuang, D.B. 0D/2D $CsPbBr_3$ Nanocrystal/BiOCl Nanoplate Heterostructure with Enhanced Photocatalytic Performance. *Adv. Mater. Interfaces* **2022**, *9*, 9. [CrossRef]
52. Borthakur, P.; Boruah, P.K.; Hussain, N.; Silla, Y.; Das, M.R. Specific ion effect on the surface properties of Ag/reduced graphene oxide nanocomposite and its influence on photocatalytic efficiency towards azo dye degradation. *Appl. Surf. Sci.* **2017**, *423*, 752–761. [CrossRef]
53. Zhou, H.; Qiu, Y.; Yang, C.; Zang, J.; Song, Z.; Yang, T.; Li, J.; Fan, Y.; Dang, F.; Wang, W. Efficient Degradation of Congo Red in Water by UV-Vis Driven $CoMoO_4$/PDS Photo-Fenton System. *Molecules* **2022**, *27*, 8642. [CrossRef] [PubMed]
54. Liang, X.; Liu, J.; Guo, H.; Li, H.; Liu, E.; Zhao, Y.; Ji, Y.; Fan, J. Preparation of a Recyclable and High-Performance Photocatalyst Agins2/Cn/Pan for Rhb and Phenol Degradation. *J. Environ. Chem. Eng.* **2023**, *11*, 3. [CrossRef]

55. Liang, Z.; Cheng, H.; Zhang, X.; Mao, Q. Two Polyoxometalates Based on {P2mo5} Catalysts: Synthesis, Characterization, and Photocatalytic Degradation of Rhb. *J. Mol. Liq.* **2023**, *377*, 121483. [CrossRef]
56. Liu, S.; Ge, Y.; Wang, C.; Li, K.; Mei, Y. Tio2/Bp/G-C3n4 Heterojunction Photocatalyst for the Enhanced Photocatalytic Degradation of Rhb. *Environ. Sci. Pollut. Res.* **2023**, *30*, 84452–84461. [CrossRef] [PubMed]
57. Smok, W.; Zaborowska, M.; Tański, T.; Radoń, A. Novel In2o3/Sno2 Heterojunction 1d Nanostructure Photocatalyst for Mb Degradation. *Opt. Mater.* **2023**, *139*, 113757. [CrossRef]
58. Athavale, S.; Barai, D.P.; Bhanvase, B.A.; Pandharipande, S.L. Investigation on Performance of Eu:Go:Ksrpo4 Nanocomposite for Mb Dye Photocatalytic Degradation: Experimental and Ann Modeling. *Optik* **2023**, *275*, 170561. [CrossRef]
59. Rastgar, S.; Rezaei, H.; Younesi, H.; Abyar, H.; Kordrostami, A. Photocatalytic Degradation of Methylene Blue (Mb) Dye under Uv Light Irradiation by Magnetic Diesel Tank Sludge (Mdts). *Biomass Convers. Biorefin.* 2023, *in press*. [CrossRef]